Journal of the European Ceramic Society xxx (xxxx) xxx

Contents lists available at ScienceDirect

Journal of the European Ceramic Society

journal homepage: www.elsevier.com/locate/jeurceramsoc

Original article

Discrete 3D modeling of porous-cracked ceramic at the microstructure scale

V. Longchamp [a,b,c,d,*], J. Girardot [b,c], D. André [d], F. Malaise [a], A. Quet [e], P. Carles [d], I. Iordanoff [b,c]

[a] CEA, DAM, CESTA, F-33114, Le Barp, France
[b] Arts et Metiers Institute of Technology, CNRS, Bordeaux INP, Hesam Universite, I2M, UMR 5295, F-33400, Talence, France
[c] Univ. Bordeaux, CNRS, Bordeaux INP, I2M, UMR 5295, F-33400, Talence, France
[d] Univ. Limoges, CNRS, IRCER, UMR 7315, F-87000, Limoges, France
[e] CEA, DAM, Le Ripault, F-37260, Monts, France

ARTICLE INFO

Keywords:
Plasma sprayed ceramics
FIB-SEM
Discrete Element Method
Porosity
Micro-cracks

ABSTRACT

The porous-cracked microstructure of plasma sprayed ceramics coatings directly influences their macroscopic mechanical response.

A 3D micromechanical model based on the discrete element method (DEM) is developed to reproduce their behavior. 3D observations are conducted with FIB-SEM nano-tomography and image analysis is used to extract and discretize the microstructure. A modeling strategy is developed to incorporate both pores and cracks into the model while preserving the computation performance. The lattice nature of DEM is used for the modeling of crack thickness that are smaller than the discrete element size. A method to compute the crack thickness from gray level images is proposed.

Virtual quasi-static tests are performed on a sample of yttria-stabilized-zirconia. The results are in accordance with the literature data, such as the anisotropy and the non-linear behavior. The model is helpful to precisely investigate the role of the microscopic components, and micro-cracking on the macroscopic failure.

1. Introduction

Plasma sprayed ceramic coatings (PSCC) are used in various industrial applications as thermal barrier and protection from corrosion or abrasion [1–3]. The thermo-mechanical properties of PSCC are directly related to their porous-cracked microstructure [4]. Such a microstructure is composed of thin irregular splats, created when melted ceramic particles impact the substrate and spread to form splats before a rapid solidification. There are small globular pores (∼1 μm) inside the splats, larger irregular pores (>1 μm) between the splats, and intra-splats and inter-splats micro-cracks (1-100 nm) [5,6]. The presence of these defects greatly affects the propagation of elastic shock waves, and contributes to their effective attenuation [7–9]. Based on this observation, the ability of PSCC to mitigate nanoseconds shock waves, driven by high velocity impact of micrometer shrapnel or high power laser experiments [10] has been investigated for few years. Research is carried with the long term objective of being able to enhance the mitigation by controlling the morphology and concentration of initial defects through process parameters.

Experimentally speaking, compressive, tensile and bending tests have been conducted to characterize the mechanical response of PSCC [11–15]. The main outcome of these studies is that the elastic modulus increases under compressive stress due to closing of micro-cracks. The sliding and internal friction of these cracks also induce some energy dissipation under cycling loading [11,16]. Moreover, an asymmetrical behavior is observed between tension and compression, as in tension the cracks tend to open and propagate, decreasing the elastic property [17]. The overall properties of PSCC depends greatly on the distribution, orientation, geometry and concentration of defects. Some constitutive relations have been proposed to describe their effect on the effective elastic modulus and elastic wave velocity [18–20]. Nevertheless, the geometry and distribution of defects are simplified and not always representative of the real microstructure, the relations are often limited to small deformations and are not able to take into account the damage evolution. Besides, a lot of parameters like crack density or crack closure pressure, defined by Kroupa [19], must be determined experimentally. Consequently, these models cannot be used to predict the behavior only from the microstructure.

To achieve this, micromechanical approaches are of real interest [21]. It concerns the direct representation of the material microstructure components into a numerical model. The pores and cracks are discretized among the solid matrix and simulations are performed to predict the macroscopic behavior of the material. The first studies were based on the Finite Element Method (FEM) to represent idealized 2D porous-cracked microstructures [6,22] or more realistic ones

* Correspondence to: I2M, Esplanade des Arts et Métiers, 33405 Talence Cedex, France.
E-mail addresses: vincent.longchamp@ensam.eu (V. Longchamp), jeremie.girardot@ensam.eu (J. Girardot).

https://doi.org/10.1016/j.jeurceramsoc.2023.11.026
Received 20 September 2023; Accepted 10 November 2023
Available online 18 November 2023
0955-2219/

through image-based modeling techniques [4,23]. Then, computation are performed to estimate mechanical properties such as the elastic modulus. However, 2D models are limited as they do not reflect the real 3D microstructure, leading to an underestimation of the mechanical properties. The transition to 3D model is a major axis of improvement, one challenge being the generation of 3D microstructure. To that end, idealized 3D microstructures are often used [24], besides volumetric observation instruments such as X-ray tomography allow carrying 3D simulations on real microstructures [25,26]. However, X-ray tomography is generally not precise enough to discriminate the smallest cracks of PSCC. The Focused Ion Beam-Scanning Electron Microscope (FIB-SEM) technique is preferred for its better resolution (down to 10 nm) [27,28]. Unfortunately, the maximal volume size is generally limited to a cube of 20 μm side. Another challenge concerns numerical modeling and management of physical phenomena: continuous methods like FEM are not necessarily the best suited to deal with complex heterogeneous microstructures, crack propagation and fragmentation induced in ceramics under quasi-static and high strain rates loading [29].

The Discrete Element Method (DEM) seems more suitable for PSCC, it was initially designed for granular media, represented as a set of discrete elements (DE), which interact together through contacts laws [30, 31]. It was afterward adapted to describe continuous media, by adding bonds that transmit cohesive forces between DE [32]. This kind of discrete representation allows to handle easily discontinuous phenomena. For instance, the propagation of cracks is usually represented by deleting bonds or elements when a failure criterion is reached, and contacts between the resulting fragments can be easily managed. These obvious advantages led to an increasing usage of DEM in the field of fracture mechanics of brittle materials, such as rock, ceramics or cements [33–35].

Some attempts to represent complex microstructures from SEM images with DEM have been proposed in literature [36,37]. In these studies, like in many others [8,9,38], pores and micro-cracks are represented by deleting DE. Although, being relatively easy and relevant for 2D modeling, this approach is not suited to the 3D discretization of PSCC that exhibits a lot of micro-cracks as it requires to use DE smaller than the micro-cracks size, inducing a considerable amount of DE which affect the computational performance. Alternative methods have been proposed to discretize small initial defects like micro-cracks. A solution is to act on the bonds, they may be removed [39] or their behavior may be modified [35,40,41]. The thickness between cracks surfaces can be taken into account by acting on the contact detection distance [42–44] or by using a variable bonds stiffness [45]. All of these works are promising and show the good capability of the DEM to simulate PSCC at the micro-scale. Nevertheless, to the author's knowledge, no investigation was found to link a small scale 3D experimental observation with a numerical modeling of the complex microstructure present in PSCC. The long term objective of this study is to investigate the behavior of Yttria-Stabilized Zirconia (YSZ) under laser driven shock wave experiments, where the nanoseconds shock waves greatly interact with the defects. The goal of this work is to set up a DEM discretization and simulation procedure of real 3D microstructure, observed thanks to FIB-SEM.

In a first section, the methodology to obtain 3D microstructural data is presented, beginning with the production of YSZ coatings, the observations thanks to FIB-SEM technique and finally the image processing and analysis involved in the detection of pores and cracks. Then, the strategy to represent the microstructure into a numerical DEM model is exposed. Finally, the influence of defects on the elastic macroscopic behavior under compression and tension is investigated through virtual quasi-static loading. The numerical results are compared to experimental data found in the literature.

2. Microstructure analysis

2.1. YSZ sample manufacture

Powder of 8 wt% Y_2O_3 stabilized ZrO_2 (8YSZ), provided by *Oerlikon metco*, is used to manufacture coating with an air plasma spray (APS) technique. This operation is performed at CEA-LR (France). The powder, made up of dense and angular particle with a median diameter (D50) of 30 μm, is sprayed on a metallic substrate. The metallic substrate is removed after the spraying in order to keep only the two millimeter thick coating. Then, the freestanding coating is machined with a diamond wire saw to obtain $6 \times 3 \times 2$ mm^3 parallelepiped specimen.

The apparent density of the specimen (ρ_P) is measured from its mass and dimension. By considering that the density of dense 8YSZ is $\rho_D = 6060\,\mathrm{kg \cdot m^{-3}}$ [46], the porosity (p_M) is estimated to be about 10% with:

$$p_M = 1 - \rho_P / \rho_D. \tag{1}$$

2.2. FIB-SEM protocol

The *ZEISS Crossbeam 550* is used to perform FIB-SEM nano-tomographic observations. It combines a Focused Ion Beam (FIB), which is used to progressively erode thin layers of the specimen, and a Scanning Electron Microscope (SEM), which acquires images between each erosion. This provides 3D high resolution visualizations of small volumes (~20^3 μm^3) by stacking all the 2D images.

2.2.1. Sample preparation

Samples preparation is essential before FIB-SEM observations, Fig. 1 shows the prepared area (1b) and the first image acquired (1c). The preparation steps consist in the deposition of a thin layer of platinum on the area that will be observed. Then, some lines are milled and filled with carbon for the tracking and auto-calibration of the FIB-SEM parameters during the acquisition. The lateral sides of the observed volume are eroded with the ion beam to reduce re-deposition problems, and a large hole is machined to reveal the observation side of the volume. The procedure is similar to the one described in [27].

2.2.2. Volume acquisition

Images are acquired with the Secondary Electrons Secondary Ions (SESI) detector with a resolution of 23.6 nm per pixel (Fig. 1c). A shearing correction is automatically applied to correct image distortion due to the angle of the electron beam relative to the imaged surface. The observation plane ($\vec{x}\vec{y}$) is perpendicular to the projection direction $\vec{z}$ (*cf.* Fig. 1a). Between each slice, a constant thickness of matter is eroded in order to get an isometric voxel size (D_{vx}) of 23.6 nm. The final raw dataset contains 899 slices with a dimension of 746 by 561 pixels, leading to a total volume of $17.61 \times 13.24 \times 21.22$ μm^3, composed of 3.76×10^8 voxels. Each slice is a gray level image encoded on 8 bits, meaning that the intensity goes from 0 (black) to 255 (white).

2.3. Data pre-processing

The image processing and 3D visualization are carried out using *Avizo 9* from *Thermo Fisher Scientific* and the open source software *ImageJ*. In a first part, a pre-processing is performed to improve images, which are contaminated by several artifacts caused by the FIB-SEM technique. The pre-processing is divided into the following steps:

(1) Alignment: A least square optimization algorithm [27] is used to ensure the best alignment of the slices.
(2) Deletion of vertical stripes: A Fast Fourier Transform (FFT) filter is used to remove the stripes in the ion beam direction ($\vec{x}$ axis).

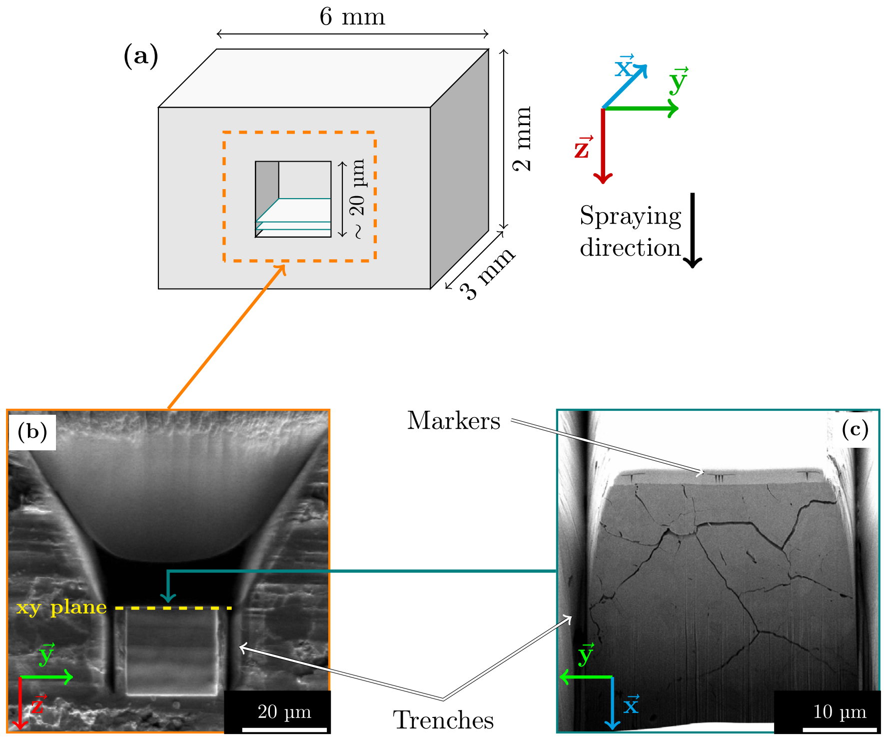

Fig. 1. FIB-SEM observation: (a) Schematic of the sample, (b) top view of the observed side and (c) image acquisition with SEM.

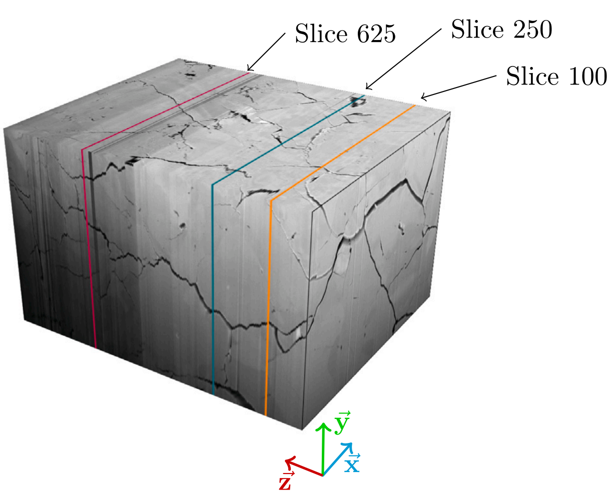

Fig. 2. 3D view of the volume and position of the slices 100, 250 and 625.

(3) Noise filtering: The non-local means (NLM) filter [47] is used for its effectiveness to smooth the noise while preserving edges sharpness. In *Avizo*, the search window and local neighborhood settings are kept on their default value of respectively 21 and 5 pixels.

(4) Intensity homogenization: The method developed by Taillon [27] is used to remove the intensity gradient in the images. It consists in resampling the data along the gradient direction and then adjust the mean intensity of each slice in order to get a constant value.

The volume after data pre-processing is shown in Fig. 2 and the successive effects of applied treatments are illustrated on three different slices in Fig. 3.

2.4. *Image processing*

Based on the observations of the previous microstructure, it is assumed to idealize the material as a set of void pores and no-thickness cracks. Segmentation and 3D morphological operations are used to extract the relevant information about porosity, they are presented in this section.

2.4.1. *Segmentation*

The segmentation consists in separating porosities from matter. The easiest way to achieve this is by applied a threshold: the value 0 (black) is assigned to all pixels whose gray level is below the selected threshold (S) and the value 255 (white) is assigned to the others, leading to binary black and white images representing respectively porosities and matter. Various methods proposed in the literature have been tested to compute automatically a threshold from the data gray level histogram. A comparison between three of them is given in Fig. 4. With *Ostu's* method [48], some thin cracks are not detected, while using the *maximum entropy* method [49], some part of the matter in the bottom corner are classified as porosities. For the present data, the preserving *moments* method [50] provide the most representative results: most cracks are detected without registering solid phase in the porosity category.

2.4.2. *Morphological operations*

Morphological operations are commonly used to separate object (groups of black voxels on a white background) according to their size [25,51]. The two fundamental operations are *erosion* and *dilation*, they induce an increase or a decrease of objects edges. These operations involve a structuring element (SE) that defines the amount of material added or removed from the edges of objects. By combining this two operations is it possible to remove only the objects smaller than the SE while keeping the initial size of the remaining ones, although their the exact shape may be altered. This is achieved with the *closing* operation, which is a *dilation* followed by an *erosion*. The principle is illustrated in Fig. 5 with a cubic SE of size 3 pixels (px).

These operations are used in the following part to classify the porosities according to their size.

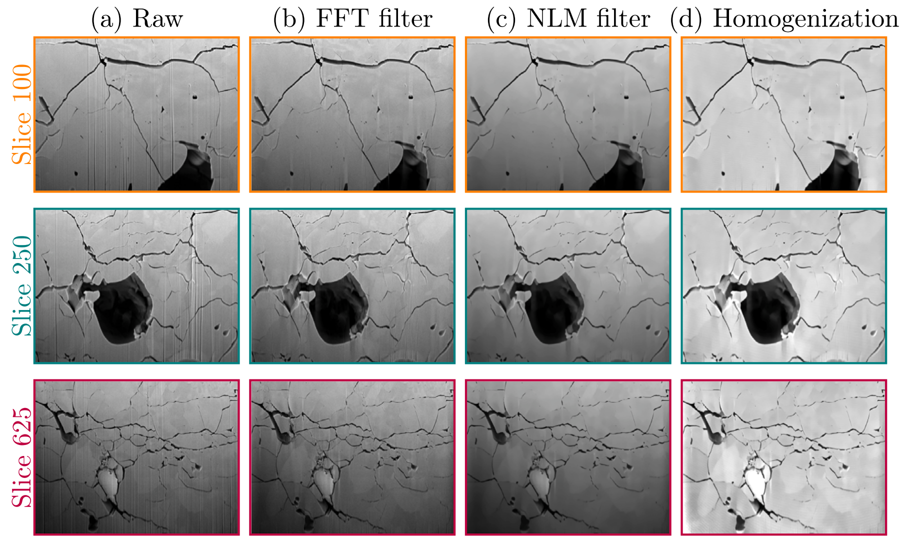

Fig. 3. Pre-processing steps on slices 100, 250 and 625 (see Fig. 2 for their positions in the volume): (a) raw image, (b) removal of vertical stripes with FFT filtering, (c) denoising with NLM filter and (d) illumination homogenization.

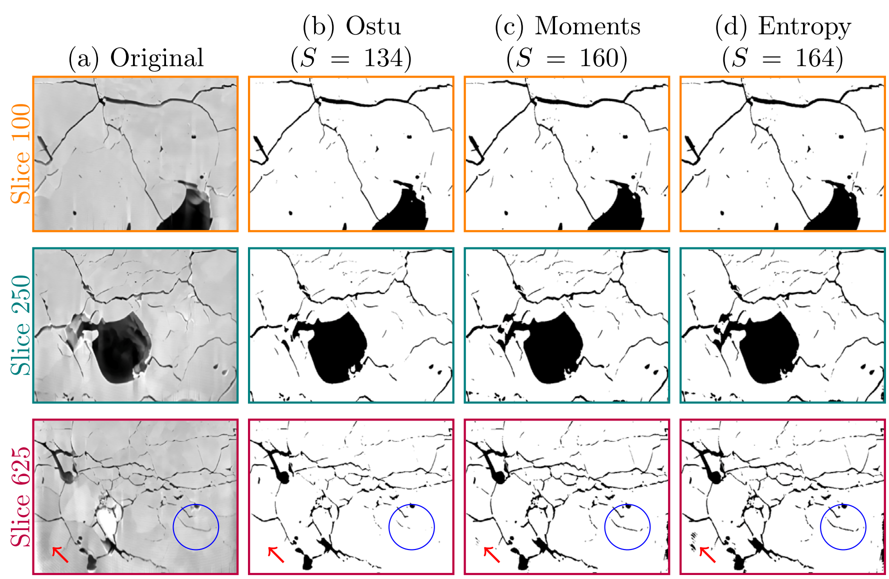

Fig. 4. Threshold (S) computed with different method, and resulting segmented image. The blue circles indicate thin cracks that are not detected with *Otsu's* method (b) and red arrows appoint matter misregistration with the *entropy* method (d).

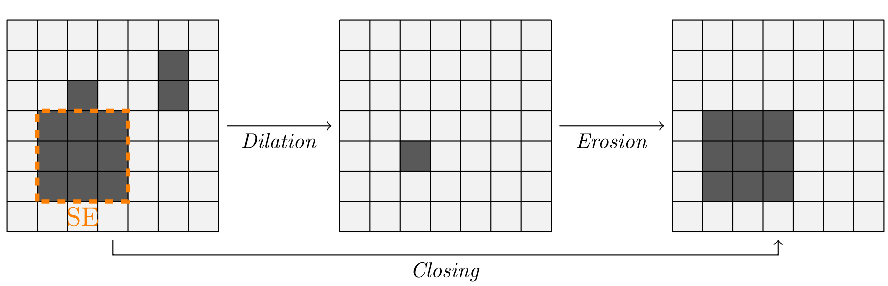

Fig. 5. 2D example of the morphological operation *Closing* where the structuring element (in dashed orange line) is a square of side 3 pixels.

2.4.3. Porosities classification

Porosities are classified in two groups according to their size [51]. Morphological and logical binary operations are used to select only the large pores and thick cracks, considered as *pores*. The *cracks* (thin cracks and small pores) are obtained by subtracting the pores from the total binary image. The complete protocol is summarized in Fig. 6 and consist of the following steps:

- Img. 0: total porosities,
- Img. 1a: *closing* operation with a ball-type SE of radius R_C to remove the smallest porosities,

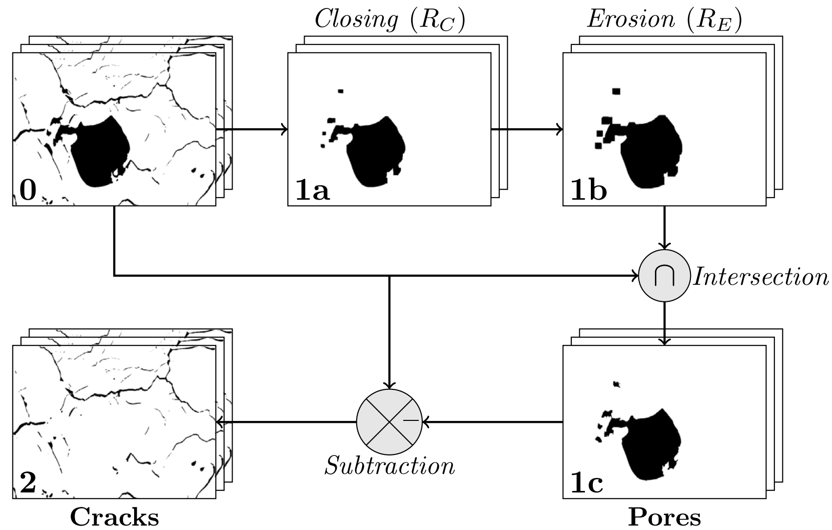

Fig. 6. Work-flow of porosities classification by image analysis.

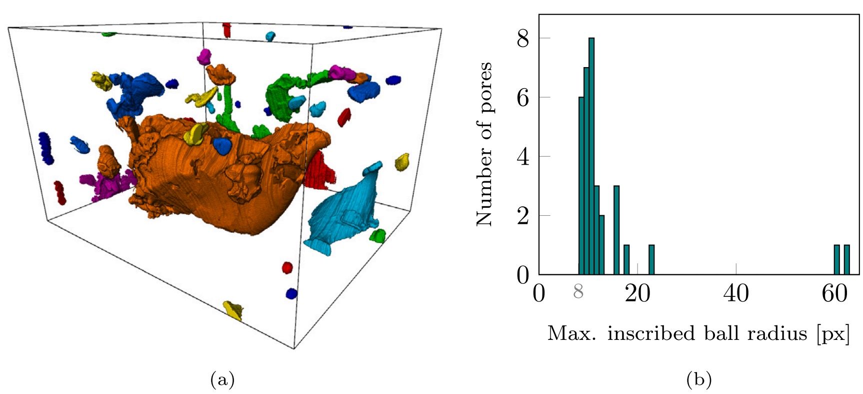

Fig. 7. (a) 3D view of pores (non-connected pores are colored in different color) and (b) histogram of the maximal inscribed ball radius in each pore.

- Img. 1b: *erosion* operation with a ball-type SE of radius R_E to enlarge the size of remaining porosities,
- Img. 1c: intersection between the enlarged porosities (img. 1b) and the total porosities (img. 0) to retrieve the exact pores geometry,
- Img. 2: subtraction of the pores (img. 1c) from the total porosities (img. 0) to obtain the cracks.

Obtaining the exact pores boundaries is essential for the extraction of cracks. In fact, performing the subtraction with (img. 1a) create some *parasitic* cracks at the edges of pores. For that reason the SE size used for the *erosion* (R_E) must be high enough to increase pore boundaries (img. 1b) beyond their initial boundaries (img. 0). The two SE radii R_C and R_E values are selected to achieve a classification where most of the thin elongated structures are classified as cracks and no parasitic cracks are created on the edge of pores. To find the best suited values, in a first part, the classification algorithm is carried out with increasing SE radius from 1.5 px to 20.5 px by considering that $R_C = R_E$. From visual inspection of the resulting classification, the value $R_C = 8.5$ px is selected, following the work of [5,36,51]. In a second part, several values of R_E from 1.5 px to 20.5 px are assessed with a constant $R_C = 8.5$ px. The value of 4.5 px is chosen because it is the smallest value that prevents parasitic cracks on the edges of pores. With these values, the pores (Fig. 7(a)) are bigger than a sphere of radius $R_C = 8.5$ px (200 nm). This is verified by computing the maximal inscribed ball radius of each porosity (Fig. 7(b)).

2.5. Crack meshing

Cracks are converted into a 3D surface with no thickness, this process is illustrated in Fig. 8. First, each image of the stack representing the cracks are *skeletonized*, this reduces the width of each object to one pixel. Then, the meshing algorithm *Alpha shape* [52] implemented in the open source software *MeshLab* [53] is used to generate a triangular mesh from the voxels coordinates of the skeleton. The mesh, which represents the crack surface, is made up of 9 million triangles.

2.6. Porosity analysis

A porosity (p_{vx}) can be computed from binary images, with the following formula:

$$p_{vx} = N_{vx}^{black} / N_{vx}^{tot}, \tag{2}$$

where N_{vx}^{black} and N_{vx}^{tot} are respectively the number of black voxels and the total number of voxels. The total porosity is $p_{vx}^{tot} = 8.83\%$, this is 12% lower than the apparent density measured with the mass (see Section 2.1). This difference is expected due to the size of the observed volume, which is too small to be representative on its own. Several volumes can be used to get statistically representative results. After the classification step, one can also compute the porosity due to pores or cracks, they are respectively equal to $p_{vx}^{pores} = 5.88\%$ and $p_{vx}^{cracks} = 2.95\%$.

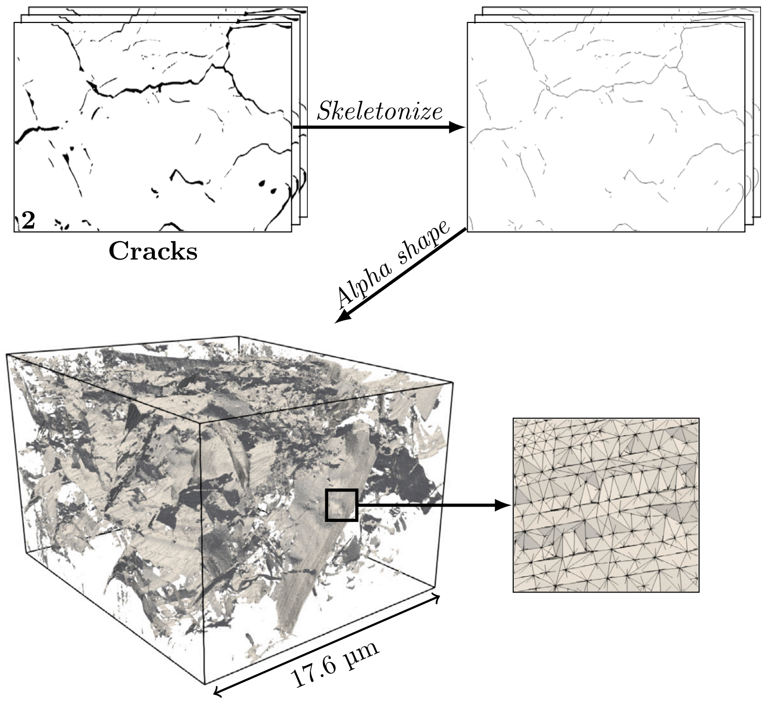

Fig. 8. Generation of a meshed surface of cracks by using skeletonize and alpha shape algorithm.

3. Discrete element modeling

In a first part, the Discrete Element method (DEM) framework used in this work is introduced, it includes the discrete domain generation and the calibration procedure. Then, the modeling strategy of pores and cracks inside a discrete domain is presented.

3.1. Discrete element method framework

DEM is used to represent a continuous medium with a set of spherical *discrete elements* (DE) connected with *bonds* that transmit cohesive forces [32]. In this work, the open source platform *GranOO* [54] is used. Based on previous works [54–56], the bond behavior is represented by cylindrical Euler–Bernoulli beams. They have a purely elastic behavior defined by four parameters (with B in subscript): E_B their elastic modulus, ν_B their Poisson's coefficient, R_B their radius and L_B their length. The beam radius is a global constant defined with respect to the mean DE radius (R_{DE}) through $\tilde{r}$, the *radius ratio* defined as:

$$R_B = \tilde{r} \times R_{DE}. \tag{3}$$

The length of each beam is implicitly set by the distance between linked DE centers, resulting in the subsequent approximation:

$$L_B \simeq 2R_{DE}. \tag{4}$$

According to the position and orientation of connected DE, tensile, bending and torsion stresses are transmitted through the beams, as illustrated in Fig. 9(a). The expression of resultant forces and momentum applied on DE can be found in [54].

DEM also allows to easily manage contact. In this work, a contact between two non-linked DE is represented by a spring repulsion law (*cf.* Fig. 9(b)):

$$F_C = K_C \times \Delta u, \tag{5}$$

where F_C is the repulsive contact force, K_C the contact stiffness and $\Delta u \geq 0$ the inter-penetration of DE. K_C is set to be equivalent to the mean beam stiffness in tensile mode:

$$K_C = \frac{E_B \times \pi \times R_B^2}{L_B}. \tag{6}$$

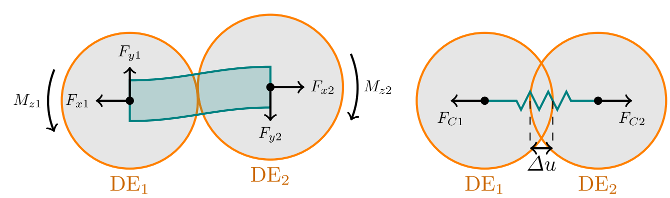

(a) Cohesive beam model (b) Contact

Fig. 9. 2D illustration of the interactions between two DE: (a) linked by a beam, and (b) through contact spring repulsion.

with Eq. (3) and (4) it becomes:

$$K_C = 0.5 \times E_B \times R_{DE} \times \pi \times \tilde{r}^2. \tag{7}$$

3.1.1. Domain generation

Initial compact domain representing dense material are generated according to the procedure described in [54]. The DE radii follows a uniform random dispersion of 25% around the selected mean DE radius R_{DE} in order to prevent the apparition of ordered arrangement that could lead to anisotropy. Then, nearest DE are connected by beams until a mean cardinality (number of beams per DE) of 6.2 is achieved. As an example, a discrete domain with $R_{DE} = 0.2$ µm is given in Fig. 10, it is composed of ~92 000 DE and ~278 000 bonds.

3.1.2. Elastic parameters calibration

The compact discrete element domain (Fig. 10), represent dense 8YSZ which is assumed to have a purely elastic linear behavior, whose parameters are given in Table 1 (the subscript D is referring to the dense material).

In DEM approach, there is no predefined relationship between the input parameters (micro-parameters) and the resulting macroscopic mechanical behavior of a domain (macro-parameters). Thus, a calibration is performed [54] to find the value of input parameters that provide the desired macroscopic behavior (Table 1) with a maximum

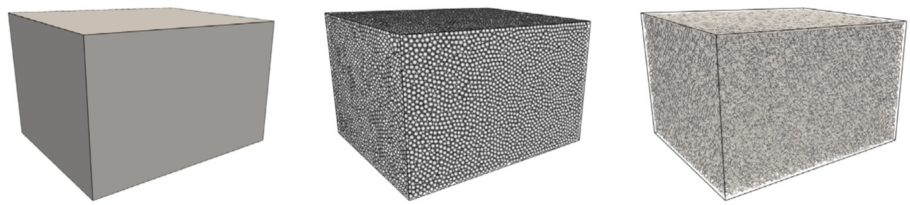

(a) Continuous volume (b) DE (c) Beams

Fig. 10. (a) An isotropic continuous volume of matter represented by (b) a set of spherical discrete elements connected with (c) cylindrical beams.

Table 1
Mechanical properties of dense 8YSZ from [46].

Macro-parameters	Sign	Value
Young's modulus	E_D	223 GPa
Poisson's coefficient	ν_D	0.29
Density	ρ_D	6060 kg/m^3

Table 2
Calibrated micro-parameters corresponding to macro-parameters of Table 1.

Micro-parameters	Sign	Value
Beam Young's modulus	E_B	5820 GPa
Beam Poisson's coef	ν_B	0.30
Radius ratio	$\tilde{r}$	0.345

difference of 1%. The resulting micro-parameters values are summarized in Table 2. The initial isotropy of the dense numerical material is verified.

3.2. Modeling strategy and selection of DE size

The ceramic coating microstructure must be reproduced into the generated dense discrete material. Usually, all the porosities are represented by deleting DE [36]. However, this requires to use DE smaller than the smallest porosity. For the present volume it would require more than 10^8 DE, which is impractical in view of the computation times involved. To overcome this limitation, only the pores (biggest porosities) are represented by deleting DE. Thus, the DE radius must be lower than the smallest pore, which size is equal to the structuring element used for classification of porosities (Section 2.4.3):

$$R_{DE} \leq R_C. \tag{8}$$

Cracks and their thicknesses (T) are represented via the bonds. Hence, the bond length (L_B) must be longer than the maximal thickness ($max(T) \leq L_B$). And, by definition of the closing operation, the maximal crack thickness is less than $2R_C$. Hence, L_B must verify:

$$T \leq 2R_C \ \leq \ L_B. \tag{9}$$

From Eq. (9), a lower bound of the DE radius can be obtained by using Eq. (4):

$$R_C \leq R_{DE}. \tag{10}$$

In order to represent both pores and cracks, the DE radius must be equal to the structuring element radius according to Eqs. (8) and (10):

$$R_{DE} = R_C. \tag{11}$$

Hence, the radius of DE is set on the value 200 nm. Fig. 11, illustrates the adopted modeling strategy: pores are represented by deleting some DE, whereas cracks are represented by modifying the behavior of beams. The following two sub-sections describe the implementation of this approach.

3.3. Representation of pores with the DE

To include pores into the discrete model, all DE whose center is inside a pore are removed, they are represented in Fig. 12. As the mass is carried by DE, removing some of them induce a decrease of the macroscopic density. A discrete porosity p_{DE} is computed from the mass of the initially dense discrete domain (M_D), and the mass of the discrete domain after the representation of pores (M_P):

$$p_{DE} = 1 - \frac{M_P}{M_D}. \tag{12}$$

The modeling of pores in the discrete model lead to a porosity $p_{DE} = 5.82\%$, which is close (1%) to the one computed from the input binary volume of the pores (*cf.* Section 2.6). The pores modeling is correct in terms of mass.

3.4. Representation of cracks with the beams

Cracks, whose thickness is smaller than the DE size, are represented by modifying the behavior of bonds. A preliminary processing is performed to localize the bonds that intersect a crack, then the strategy to introduce and compute a local crack thickness in bonds is described.

An intersection detection algorithm is used to detect all bonds crossed by a crack, they are represented in Fig. 13. The Linked Cell Method (LCM) algorithm is adopted to optimize the detection. It was originally developed for contact detection [57], and is here adapted to the bond-mesh (*ie.* segment-triangle) intersection. This algorithm, combined with the skeletonize operation, improves greatly the computation time which is estimated to be at least 700 times faster than a brute force method.

3.4.1. Crack thickness modeling

Cracks can be represented by removing bonds in the initial dense domain [39–41]. However with such a representation, cracks are assumed to have zero thickness as the DE are initially in contact. Based on the work of [42], the crack thickness can be represented through the modification of bond behavior. In this work, a new kind of bond is implemented: the *Contact Beam* (CB). They only work in compression by transmitting repulsive normal force to mimic a contact behavior without friction (no tangential forces nor moments are transmitted). A comparison of the tension–compression behavior of beam and contact-beam is given in Fig. 14. By defining the compressive state of CB when their current length L is below a *contact length* L_C, a thickness T is introduced:

$$L_C = L_0 - T, \tag{13}$$

with L_0 the initial length.

To the authors' knowledge, no method for calculating this thickness has been proposed, and a calibration from experimental results is required. In order to avoid the use of a calibration, a thickness estimation method is proposed in the following section.

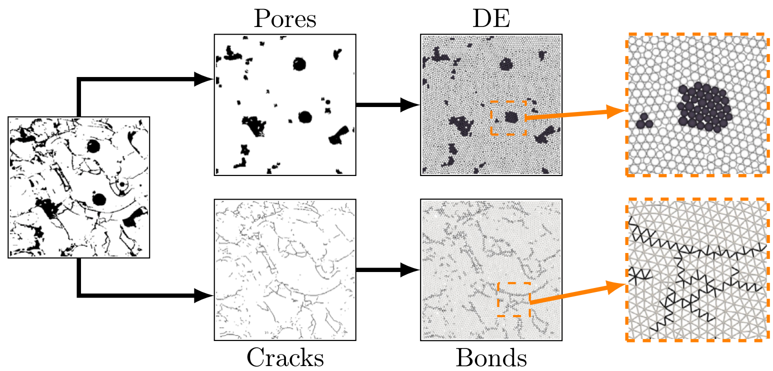

Fig. 11. Discretization procedure : from real microstructure to virtual DEM microstructure. DE on pores and bonds intersecting cracks are represented in black.

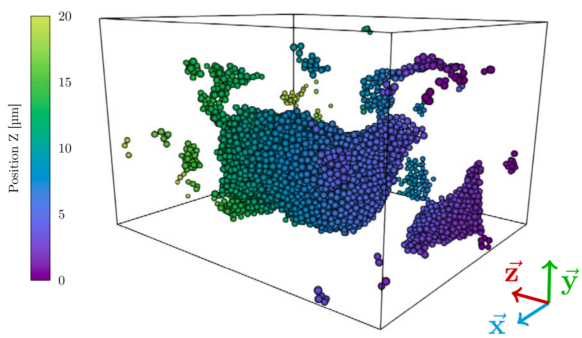

Fig. 12. 3D view of all the discrete elements that are removed to represent the pores (color gradient indicate the position along the $\vec{z}$ axis).

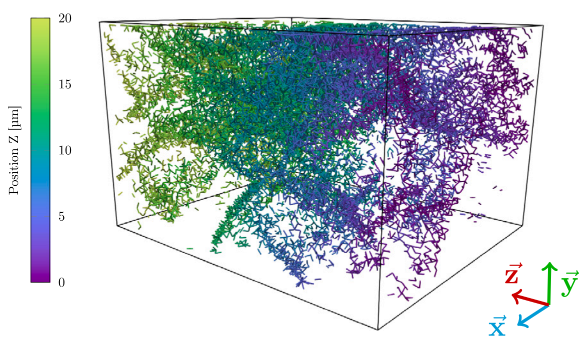

Fig. 13. 3D view of all the bond that intersect a crack surface (color gradient indicate the position along the $\vec{z}$ axis).

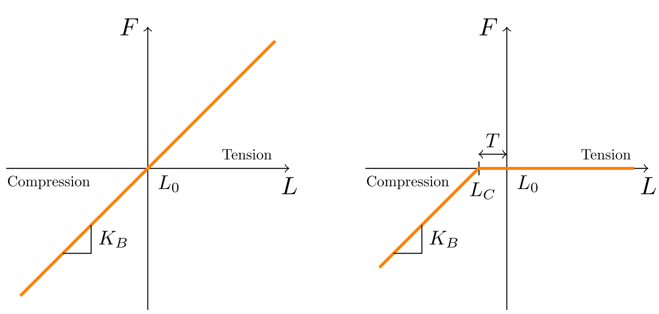

(a) Beam (b) Contact-Beam

Fig. 14. Normal force (F) as a function of length (L) for the standard GranOO *Beam* (a) and the *ContactBeam* (b) (K_B is the normal stiffness of the beam).

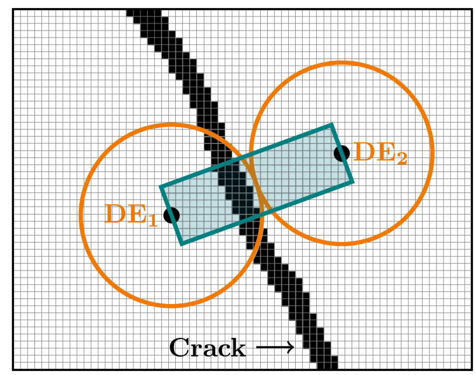

Fig. 15. Illustration in 2D of the calculation method used to assess the thickness T_1 of a bond (in green) linking elements DE_1 and DE_2.

3.4.2. *Determination of crack thickness by image analysis*

Each beam that intersects a crack is replaced by a contact beam. For each of these CB, one must compute the thickness value to input into the CB. This thickness depends on the position of the beam and its orientation with respect to the crack. Considering CB as cylinders, a computing method based on the voxels inside CB is proposed.

In a first approach, a *binary method*, noted T_1, is considered:

$$\frac{T_1}{L_0} = \frac{N_{vx}^{black}}{N_{vx}^{tot}}, \tag{14}$$

with N_{vx}^{tot} the total number of voxel inside the considered bond and N_{vx}^{black} the number of black voxel inside the bond. A 2D example of this computation method is given in Fig. 15, where $N_{vx}^{black} = 28$ px, $N_{vx}^{tot} = 225$ px and $L_0 = 25$ px, leading to $T_1 = 3.1$ px. This binary method shows a direct a drawback due to its voxel size dependency. Indeed, the minimum crack thickness is driven by the voxel size.

Hence, another method, based on the original non-binarized volume is proposed in order to be voxel size independent. This *intensity method* (T_2) involves the average normalized intensity level (I_i/S) of voxels representing cracks, *ie.* voxels whose gray level are below the threshold S (denoted $N_{vx}^{<S}$):

$$\frac{T_2}{L_0} = \frac{1}{N_{vx}^{tot}} \times \sum_{i=1}^{N_{vx}^{<S}} \left(1 - \frac{I_i}{S}\right). \tag{15}$$

Fig. 16 compares the results given by the two methods for different increasing voxel size (D_{vx}) on the same volume. The histograms put forward the voxel size dependency of the binary method with an increase of computed values T_1 when D_{vx} increase, unlike the intensity method which gives the same results T_2 regardless of voxel size. Moreover, the distribution computed with the intensity method present a typical rise in density for decreasing values of thickness, even below the

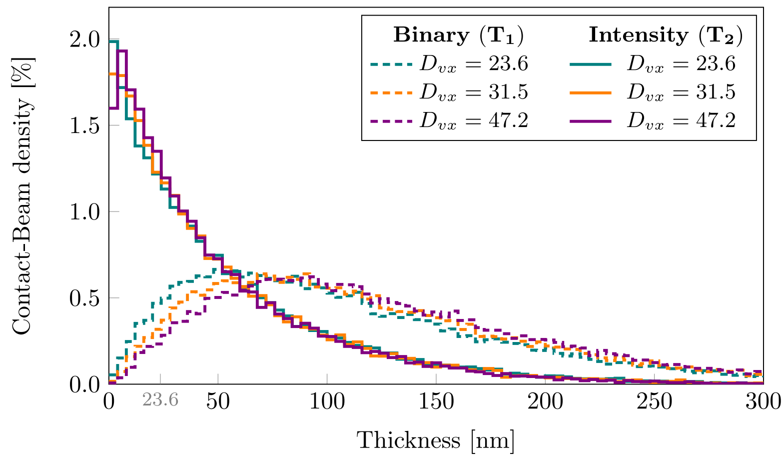

Fig. 16. Histogram (bar width=4 nm) of thicknesses computed with the *binary* method (dashed)) and *intensity* method (solid), for various voxel size D_{vx} (in nanometer).

voxel size, which is generally expected when considering population of defects [58]. For these reasons, the *intensity* method is selected in the rest of this study

4. Anisotropy and non-linear behavior assessment

Plasma sprayed ceramics exhibits complex macroscopic mechanical behavior, with:

- Anisotropy due to the preferential crack orientation, inter-splat cracks lead to a lower elastic modulus in the direction of the plasma projection [59,60],
- Asymmetry between tensile and compressive loading is reported [12,13],
- Non-linear behavior under compression loading due to the progressive closing of cracks [12,16],
- Dissipative behavior during cycled loading due to friction of crack surfaces [11,61].

Although the friction between cracks surface is not considered in this work, the ability of the developed 3D DEM model to reproduce the complex behavior of PSCC is investigated by performing numerical quasi-static loading tests. In a first part, uniaxial tests are used to study the anisotropy and asymmetry. In a second part, triaxial compression loading tests are performed to study the effect of microstructure on pressure–density law. Finally, cycled loading are applied with the use of a cracking criterion.

4.1. Anisotropy and asymmetry

4.1.1. Numerical loading description: uniaxial loading

Uniaxial tensile and compressive numerical tests are performed on the virtual microstructure in the three directions of space. The applied loading and boundary conditions are described in Fig. 17. For a given direction $\vec{i} \in \{\vec{x}, \vec{y}, \vec{z}\}$, a normal displacement (D_{load}) is imposed on one side of normal $\vec{i}$, while the normal displacement of the opposite side is fixed ($\vec{D} \cdot \vec{i} = \vec{0}$). The displacement of the others sides are free. The mean resulting force $\vec{F_i}$ applied on both loaded faces is used to compute the normal stress σ_{ii} (Eq. (16)), and the dimension of the sample is used to compute the axial and transversal strains (Eq. (17)):

$$\sigma_{ii} = \frac{\vec{F_i} \cdot \vec{i}}{S_{0i}}, \tag{16}$$

$$\epsilon_{ii} = \frac{L_i - L_{0i}}{L_{0i}}, \tag{17}$$

where L_i is the dimension of the sample along the $\vec{i}$ axis, S_i is the section of normal $\vec{i}$ and 0 in subscript is used to refer to initial values.

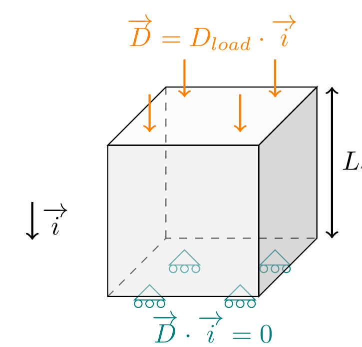

Fig. 17. Uniaxial loading configuration along $\vec{i}$ axis.

4.1.2. Asymmetry analysis

Stress–strain curves for each direction under tensile and compressive loading are plotted in Fig. 18. Under tensile loading, the behavior is linear. Conversely, under compressive loading the behavior is non-linear with an increasing stiffness in relation with the applied axial strain. This asymmetric behavior, between tensile and compressive loading, is due to the closing of intra and inter-splats cracks that only occurs under compression [19]. An example of the displacement field under a compressive loading along the y-axis at an axial strain of −0.59% is shown in Fig. 19. This picture clearly highlights the influence of cracks on the displacement field, which is not uniform because of the crack thickness. It also demonstrates the interest of using DEM in order to deal with all the contact management induced by the discontinuities in compression. The effect of cracks on the non-linear behavior is explored more in depth in Section 4.2.

4.1.3. Anisotropy analysis

Anisotropy is visible in Fig. 18 with a different response for each direction. To quantify this difference, the stress–strain curves at small strain (0.1%) are used to compute the Young's modulus. In the linear range, the values are equal under tensile and compression, they are reported in Table 3. Additional computations have been performed to discriminate the contribution of each defect (pores and cracks), the results are also reported in Table 3, where the elastic modulus in the spraying direction ($\vec{z}$ axis, see Fig. 1) is the longitudinal modulus (E_L), while the modulii in the two other orthogonal directions are the transverse modulii (E_T).

Transverses Young's modulii are close to the upper bound of literature data (~ 90 GPa). However, the longitudinal modulus is twice higher than literature data (~ 60 GPa) [4,16,60]. The level of anisotropy

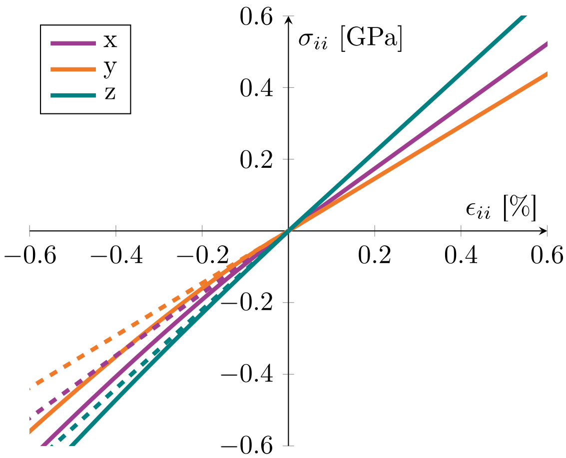

Fig. 18. Stress–strain curves for tensile and compressive loading (dashed line represent the tangent at the origin to put forward the non-linear behavior in compression).

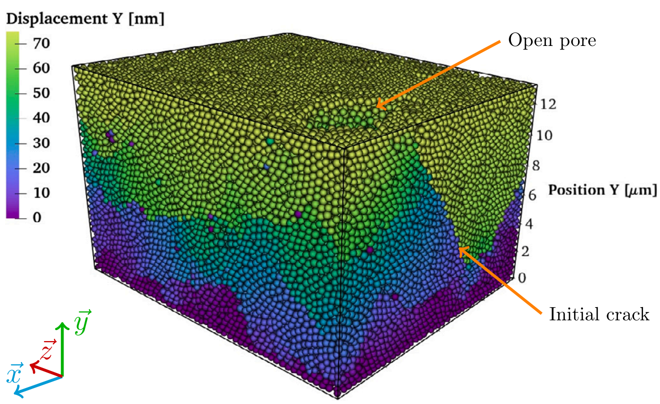

Fig. 19. Displacement field under uniaxial compressive loading along the y-axis at $E_{yy} = -0.59\%$.

Table 3
Elastic moduli in the three directions of space for each microstructure components.

	E_{T_X} [GPa]	E_{T_Y} [GPa]	E_{L_Z} [GPa]
Pores and cracks	89	74	115
Cracks without pores	135	111	159
Pores without cracks	186	184	190
Bulk	223	223	223

can be quantified with the ratio of transverse modulus over longitudinal modulus (E_T/E_L). Transverses modulii are smaller than the longitudinal one, with $E_{T_X}/E_L = 77\%$ and $E_{T_Y}/E_L = 64\%$. Literature data report a different trend, with longitudinal modulus lower than transverse one ($E_T/E_L > 100\%$). According to [4,16,60], this trend is attributed to the presence of inter-splat cracks, orthogonal to the spraying direction ($\vec{z}$), that play a greater role in reducing the modulus than inter-splat cracks in the transverse direction. The overestimation of the current model may come from its dimension that are not sufficient to capture well the effect of inter-splat cracks. Indeed, the dimension of a splat is around 20 μm in thickness and about 100 μm in radius. In the present study, the volume (20 × 20 × 20 μm^3) is hence too small to capture accurately the effect of those macro inter-splat cracks.

As a summary, the transverse modulii, that are mainly affected by the numerous small intra-splat cracks, are in good accordance with literature data. It supports the relevance of such a model, which is able to take into account the presence of cracks despite their small thickness. Nonetheless, a larger volume of matter is require to improve the representation of inter-splat cracks and get better longitudinal modulus prediction.

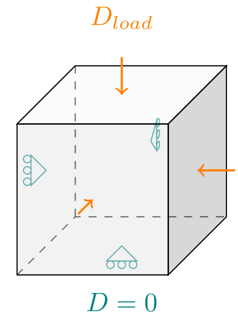

Fig. 20. Triaxial loading configuration.

Simulations on virtual microstructure containing only pores or only cracks are used to study the origin of anisotropy. The sample containing only pores shows an isotropic behavior with elastic modulus equal in the three directions of space as $E_{T_X}/E_L = 98\%$ and $E_{T_Y}/E_L = 97\%$. Conversely, anisotropy is observed in sample containing only cracks with $E_{T_X}/E_L = 85\%$ and $E_{T_Y}/E_L = 70\%$. These results confirm that the cracks are responsible for the mechanical anisotropy of the numerical sample due to their preferential orientation. This is in line with the results of other studies [19,36,60].

As a verification, a theoretical Young's modulus (E_{th}) is computed with Eq. (18) from [62] and compared to the mean modulus of the virtual material containing only pores.

$$\frac{E_{th}(p)}{E_D} = 1 - p\frac{3(1-\nu_D)(9+5\nu_D)}{2(7-5\nu_D)}. \tag{18}$$

where E_D and ν_D are the Young's modulus and Poisson's coefficient of the dense material (*cf.* Table 1). And p is the porosity, here equal to 5.82% (see Section 3.3). Theoretical (197 GPa) and numerical (187 GPa) Young's moduli differ by 5%, this is reasonably limited considering all the assumption of the theoretical formula, and confirm the good modeling of the pores inside the numerical volume.

4.2. Non-linear behavior in compression

4.2.1. Numerical test description: triaxial loading

Numerical triaxial compression tests are performed by applying the same displacement simultaneously in the three directions of space as shown on Fig. 20. In order to compute the pressure–density thermodynamic law, the macroscopic hydrostatic pressure P_h is computed from the diagonal components of the macroscopic stress tensor (Eq. (16)), with:

$$P_h = -\frac{1}{3} \times \mathrm{tr}\left(\sigma_{xx} + \sigma_{yy} + \sigma_{zz}\right). \tag{19}$$

The normalized density η is computed thanks to the current (V) and initial (V_0) volume of the domain:

$$\eta = \frac{\rho - \rho_0}{\rho_0} = \frac{V_0 - V}{V}, \tag{20}$$

$$V = L_x \times L_y \times L_z. \tag{21}$$

The tangent bulk modulus K is estimated with:

$$K = -V\frac{dP}{dV} = \eta\frac{dP}{d\eta}. \tag{22}$$

The amount of crack closure is evaluated by defining a dimensionless variable γ:

$$\gamma = \frac{N_{CB}^{comp}}{N_{CB}^{tot}}, \tag{23}$$

where N_{CB}^{tot} is the number of CB and N_{CB}^{comp} is the number of CB in compression (*ie.* with $L < L_C$).

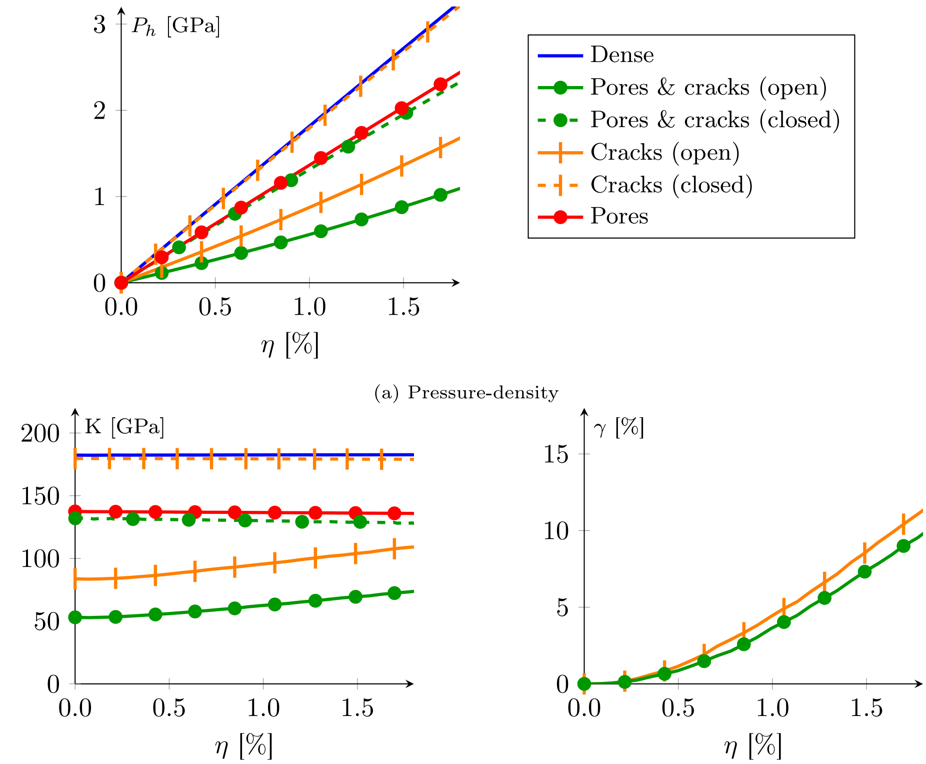

(a) Pressure-density

(b) Tangent modulus

(c) Crack closure

Fig. 21. (a) Pressure–density law, (b) Tangent bulk modulus and (c) Crack closure of several virtual microstructures containing pores and/or cracks that are open or closed.

4.2.2. Analysis of the effect of pores and cracks

The numerical triaxial tests are performed on various virtual materials containing no pores nor cracks (dense), pores without cracks, cracks without pores or both pores and cracks. When cracks are present, two cases are considered, one where they have zero thickness (closed) and one where they have a thickness (open). The numerical results are presented in Fig. 21.

As expected, the behavior with pores and open cracks is non-linear (green solid line on Fig. 21(a)). This non-linearity can be quantified with an increase of the bulk modulus from 52 GPa at $\eta = 0\%$ to 70 GPa at $\eta = 1.5\%$ (Fig. 21(b)). This increase in tangent bulk modulus correlates directly with progressive crack closure observed on Fig. 21(c). At the relaxed state ($\eta = 0\%$), all the cracks are open ($\gamma = 0\%$). Increasing pressure causes some cracks to close which lead to an increase of the bulk modulus. The non-linear tendency is only observed in virtual microstructures containing open cracks. Indeed, when there are only pores (red curve) or when the cracks are closed (dashed curves) the behavior is linear. Actually, the presence of closed cracks has a negligible effect on the compressive mechanical response. In addition, to investigate the contribution of pores and open cracks, the initial bulk modulii are compared with respect to the bulk modulus of the dense material (K_D):

- with only pores $K_P/K_D = 75\%$,
- with only cracks $K_C/K_D = 46\%$,
- with both pores and cracks $K_{P+C}/K_D = 29\%$.

The relative bulk modulus with pores and cracks is lower than the cumulative independent contributions of pores and cracks ($K_P/K_D \times K_C/K_D = 35\%$). Hence, there is a coupling effect between pores and cracks on the mechanical behavior, and both populations of defects cannot be considered independently. It put forward the relevance of this model which is able to represent simultaneously both pores and cracks despite their high size difference.

4.2.3. Analysis of the influence of the crack thickness

To study more in-depth the effect of crack thickness on the mechanical non-linearity, virtual microstructures with only cracks of various thicknesses values are considered. Pores are not represented to simplify the analysis and instead of the automatic thickness computation method presented in Section 3.4.2, here the thickness of all CB is fixed at a constant value. The results are presented in Fig. 22 for thicknesses values between 0 nm and 100 nm. For comparison purpose, two other case are represented: no crack (blue line) and crack thickness computed with the intensity method T_2 from Section 3.4.2 (dashed red line).

The thickness value greatly affects the resulting behavior. As expected, the more the thickness value is small, the more the behavior (Fig. 22(a)) is close to the one of the dense material with no cracks. Indeed, the smaller the thickness is, the faster the cracks are closing, as visible on Fig. 22(c) with γ reaching 100% and the bulk modulus reaching a maximal value close to the one of the dense material on Fig. 22(b). This is in accordance with Kroupa's theory [19], that correlate the crack closure with their aspect ratio (ratio of crack surface to their thickness).

The constant thickness that fit the best the behavior obtained with T_2 (dashed red curve) is 40 nm, this is expected as the median value of the distribution obtained with T_2 is 37 nm. However, with T_2 the cracks begin to close as soon as pressure increases, this is caused by the distribution of thicknesses values from 0 nm to 400 nm (*cf.* Fig. 16). The thinnest cracks are responsible for the non-linear behavior at the lowest pressure. For constant thickness value above 10 nm a first linear part is clearly distinguishable, as cracks surfaces are getting closer without touching and the non-linear response begins when some crack surface come into contact.

Finally, one can observe that the modulus reaches its maximum before all the CB enter in compression, for instance in the 2 nm case, the modulus reach its maximum when $\eta = 1\%$ whereas all the CB are not in compression $\gamma(\eta = 1\%) = 90\%$. Accordingly, one can conclude that the thinnest cracks that are the first to close have more influence on the non-linear behavior than the thickest cracks.

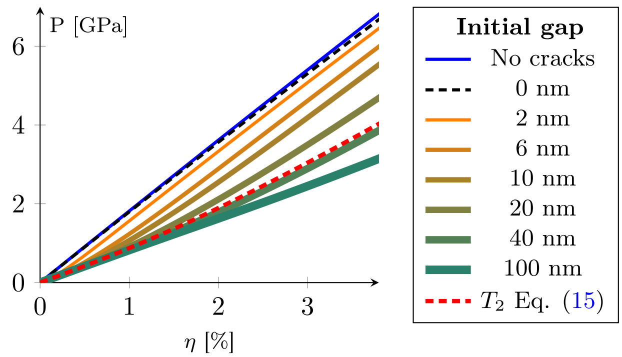

(a) Pressure-density

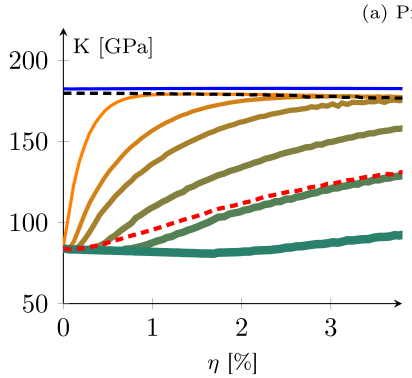

(b) Tangent bulk modulus

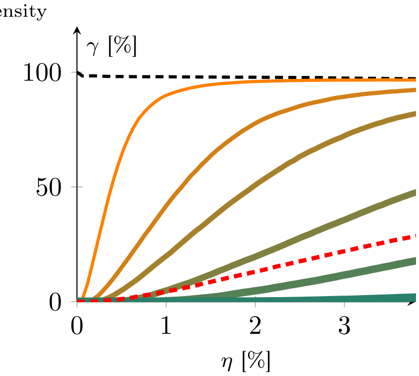

(c) Crack closure

Fig. 22. Comparison of the behavior with only cracks of different thickness: (a) Pressure–density law, (b) Tangent bulk modulus and (c) Crack closure.

4.3. Crack initiation and propagation

One motivation of using DEM is also its ability to naturally handle activation and propagation of cracks. The effect of cracking on the behavior and its relation with the microstructure is explored in this section.

4.3.1. Cracking implementation

New cracks are usually created by deleting elements or bonds [36, 63]. To be consistent with the modeling proposed in this paper, a cracking process using the contact-beam model is implemented: cracks creation and propagation is handled by converting beam into contact-beam.

The conversion of a beam is activated when it reaches a certain stress threshold. Since beams are subjected to compound stresses (tensile, bending and torsion), an equivalent stress σ_R is constructed using Rankine's formula:

$$\sigma_R = \frac{1}{2}\left(\sigma_{N max} + \sqrt{\sigma_{N max}^2 + 4\tau_{max}^2}\right). \tag{24}$$

where $\sigma_{N max}$ is the maximal normal stress in the beam (sum of tensile and maximal bending stress) and τ_{max} is the maximal torsion stress in the beam [63]. Beams are converted to contact-beam when their Rankine stress reaches a predefined threshold value ($\sigma_R \geq \sigma_{failure}$). The ratio of contact-beam number N_{CB} over the bond number N_B (which is constant equal to the sum of beams and contact-beams) is used to follow the global cracking evolution:

$$\alpha = \frac{N_{CB}}{N_B}. \tag{25}$$

4.3.2. Monotonic uniaxial loading

To study the effect of cracking on the behavior, uniaxial loading tests are carried for various bond stress failure between 10 and 50 GPa (note that the bond stress failure is a micro-parameter different from the effective macroscopic failure stress). The results are presented in Fig. 23, each curve corresponds to two different tests: one in compression and one in tension. The stress–strain curves (Fig. 23(a)) exhibit a brittle behavior, both in tensile and compression there are sudden failure, the ultimate failure stresses in tensile (UTS) and compression (UCS) are reported in Table 4. UCS values are higher by a factor 3 than UTS values.

Table 4
Ultimate Tensile Strength (UTS) and Ultimate Compression Strength (UCS) for various bond failure stresses $\sigma_{failure}$.

$\sigma_{failure}$ [GPa]	10	20	30	40	50
UTS [MPa]	61	120	179	243	308
UCS [MPa]	171	345	540	753	1002
UCS/UTS	2.8	2.88	3.02	3.10	3.25

Concerning the cracking evolution on Fig. 23(b), for each value of $\sigma_{failure}$ the same amount of CB are created after the macroscopic failure. However, the cracking is not the same in tensile and compression: more cracks are created in compression (4.4% new CB) than in tensile (1% new CB). The state of the samples after failure are presented in Fig. 24. In tensile there is a unique macro-crack perpendicular to the loading direction, whereas in compression there are multiple cracks.

4.3.3. Cycled uniaxial loading

To study the damage evolution, a cycled loading is applied on the samples. The cycled response curves plotted on Fig. 25 follows the envelope of the monotonous loading (in dashed black line). The stiffness decreases at the unloading of each cycle, due to the cracking propagation during each loading. Unloading are linear, and no residual strain is observed at the end of the unloading, this is attributed to the absence of friction in the model.

This kind of simulation can be used to identify the corresponding damage model that could be used in macroscopic homogeneous model, with for example the use of progressive damage law in the bond [55].

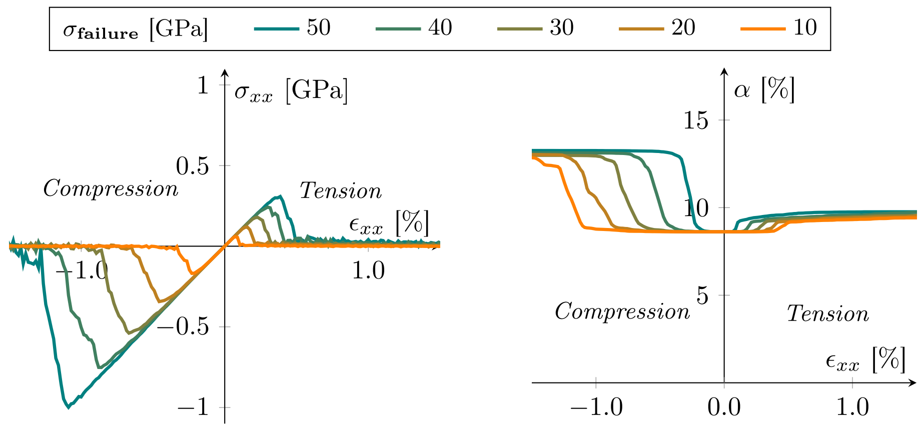

(a) Stress-Strain (b) Cracking evolution

Fig. 23. (a) Stress–strain curves and (b) cracking evolution, under uniaxial loading in tensile and compression along $\vec{x}$ for various failure stresses $\sigma_{failure}$.

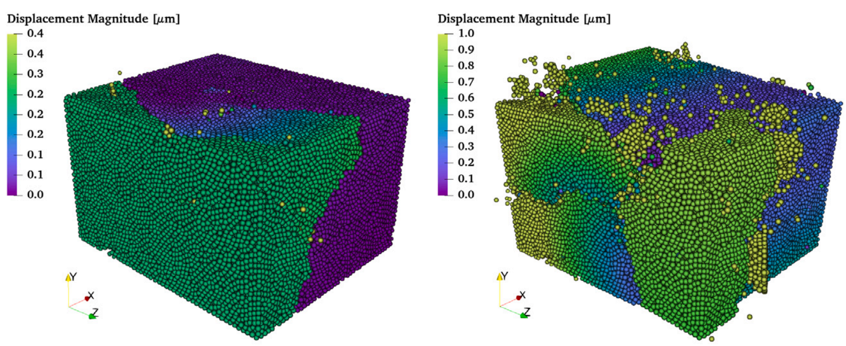

(a) Tensile (b) Compression

Fig. 24. Displacement field in the sample under uniaxial loading at $|E_{xx}| = 1.33\%$ for $\sigma_{failure} = 30$ GPa.

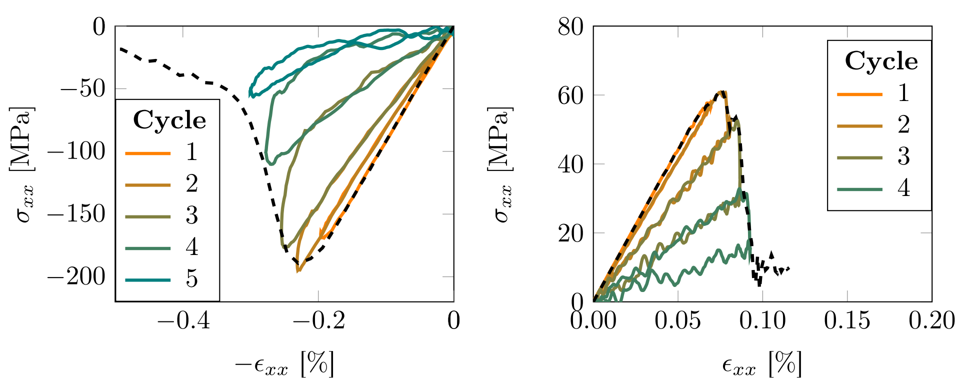

(a) Compressive loading (b) Tensile loading

Fig. 25. Cycled uniaxial loading along x-axis for $\sigma_{failure} = 10$ GPa (monotonic loading represented in dash).

5. Conclusions

A methodology to numerically reproduce the complex 3D microstructure of plasma sprayed ceramic coating with the discrete element method has been developed. It relies on 3D FIB-SEM observations to faithfully discretize the pores and the exact crack geometry. Cracks and their nanometric thicknesses are modeled through the modification of the bond behavior. Their thickness is computed by image analysis, so that calibration is not required. Hence, the only input of the model are the 3D observations and properties of the dense ceramic matrix.

The methodology has been applied to a small volume of plasma sprayed YSZ. Numerical quasi-static loading are used to characterize the mechanical behavior. The model is able to capture the anisotropy of the material and is used to confirm that the cracks are responsible for this anisotropy. The typical non-linear behavior in compression is also successfully reproduced thanks to the crack thickness representation. A coupled effect between pores and cracks has also been put forward as they both interact to decrease the elastic modulus. The DEM's ability to represent cracking is exploited to perform fracture testing. As expected, the behavior is brittle both in traction and compression, but variation are observed in ultimate strength values and failure pattern. Cycled loading can also be used to identify macroscopic damage law induced by cracking at the microscale. These qualitative results are encouraging, and triaxial compressions with cracking are planned in order to get pressure–density relationship that can be used as homogenized laws in simulation at the macroscopic scale.

Besides, the developed model is a useful tool to study precisely the influence of the microstructure on the mechanical behavior, for instance by using different distribution of crack thicknesses. The methodology could also be extended to design artificial microstructure, and comparison between different plasma sprayed microstructure are planned.

Different axis of improvement relies on the use of bigger volume of matter to obtain more representative results, this would be possible with the rising plasma-FIB technology and high-performance computing. The use of more sophisticated image processing techniques like threshold methods based on gradient or machine learning could also improve the microstructure analysis and its discretization. Finally, internal stresses and the friction at the cracks interfaces could be implemented into the model to increase its accuracy. The effect of more sophisticated cracking criterion is also under investigation.

Declaration of competing interest

The authors declare that they have no known competing financial interests or personal relationships that could have appeared to influence the work reported in this paper.

Acknowledgments

This work was supported by the French Alternative Energies and Atomic Energy Commission (CEA); and Région Nouvelle-Aquitaine.

References

[1] A. Keyvani, Microstructural stability oxidation and hot corrosion resistance of nanostructured Al2O3/YSZ composite compared to conventional YSZ TBC coatings, J. Alloys Compd. 623 (2015) 229–237, http://dx.doi.org/10.1016/j.jallcom.2014.10.088.

[2] R.S. Lima, B.M.H. Guerreiro, M. Aghasibeig, Microstructural characterization and room-temperature erosion behavior of as-deposited SPS, EB-PVD and APS YSZ-based TBCs, J. Therm. Spray Tech. 28 (1–2) (2019) 223–232, http://dx.doi.org/10.1007/s11666-018-0763-6.

[3] S. Tao, J. Yang, F. Shao, H. Zhao, X. Zhong, Y. Zhuang, J. Sheng, J. Ni, Q. Li, S. Tao, Atmospheric plasma sprayed thick thermal barrier coatings: Microstructure, thermal shock behaviors and failure mechanism, Eng. Fail. Anal. 131 (2022) 105819, http://dx.doi.org/10.1016/j.engfailanal.2021.105819.

[4] Z. Wang, A. Kulkarni, S. Deshpande, T. Nakamura, H. Herman, Effects of pores and interfaces on effective properties of plasma sprayed zirconia coatings, Acta Mater. 51 (18) (2003) 5319–5334, http://dx.doi.org/10.1016/S1359-6454(03)00390-2.

[5] S. Deshpande, A. Kulkarni, S. Sampath, H. Herman, Application of image analysis for characterization of porosity in thermal spray coatings and correlation with small angle neutron scattering, Surf. Coat. Technol. 187 (1) (2004) 6–16, http://dx.doi.org/10.1016/j.surfcoat.2004.01.032.

[6] A. Kulkarni, Z. Wang, T. Nakamura, S. Sampath, A. Goland, H. Herman, J. Allen, J. Ilavsky, G. Long, J. Frahm, R. Steinbrech, Comprehensive microstructural characterization and predictive property modeling of plasma-sprayed zirconia coatings, Acta Mater. 51 (9) (2003) 2457–2475, http://dx.doi.org/10.1016/S1359-6454(03)00030-2.

[7] D. Grady, Analytic solutions and constitutive relations for shock propagation in porous media, in: AIP Conference Proceedings. Vol. 706, AIP, Portland, Oregon (USA), 2004, pp. 205–208, http://dx.doi.org/10.1063/1.1780217.

[8] Y. Yu, X. Cao, J. Yang, Y. Li, W. Wang, H. He, Delayed fracture of porous ceramics under shock-wave compression, Eng. Fract. Mech. 208 (2019) 38–44, http://dx.doi.org/10.1016/j.engfracmech.2019.01.001.

[9] Z. Jiang, G. Gao, X. Xiong, Y. Wang, Mechanical response and deformation mechanisms of porous PZT95/5 ceramics under shock-wave compression, J. Eur. Ceram. Soc. 41 (2) (2021) 1251–1262, http://dx.doi.org/10.1016/j.jeurceramsoc.2020.09.051.

[10] J.L. Bourgade, R. Marmoret, S. Darbon, R. Rosch, P. Troussel, B. Villette, V. Glebov, W.T. Shmayda, J.C. Gomme, Y. Le Tonqueze, F. Aubard, J. Baggio, S. Bazzoli, F. Bonneau, J.Y. Boutin, T. Caillaud, C. Chollet, P. Combis, L. Disdier, J. Gazave, S. Girard, D. Gontier, P. Jaanimagi, H.P. Jacquet, J.P. Jadaud, O. Landoas, J. Legendre, J.L. Leray, R. Maroni, D.D. Meyerhofer, J.L. Miquel, F.J. Marshall, I. Masclet-Gobin, G. Pien, J. Raimbourg, C. Reverdin, A. Richard, D. Rubin de Cervens, C.T. Sangster, J.P. Seaux, G. Soullie, C. Stoeckl, I. Thfoin, L. Videau, C. Zuber, Diagnostics hardening for harsh environment in laser Mégajoule (invited), Rev. Sci. Instrum. 79 (10) (2008) 10F301, http://dx.doi.org/10.1063/1.2991161.

[11] V. Harok, K. Neufuss, Elastic and inelastic effects in compression in plasma-sprayed ceramic coatings, J. Therm. Spray Technol. 10 (1) (2001) 126–132, http://dx.doi.org/10.1361/105996301770349592.

[12] S.R. Choi, D. Zhu, R.A. Miller, Mechanical properties/database of plasma-sprayed ZrO2-8wt% Y2O3 thermal barrier coatings, Int. J. Appl. Ceram. Technol. 1 (4) (2005) 330–342, http://dx.doi.org/10.1111/j.1744-7402.2004.tb00184.x.

[13] T. Wakui, J. Malzbender, R. Steinbrech, Strain dependent stiffness of plasma sprayed thermal barrier coatings, Surf. Coat. Technol. 200 (16–17) (2006) 4995–5002, http://dx.doi.org/10.1016/j.surfcoat.2005.05.001.

[14] Y. Liu, T. Nakamura, V. Srinivasan, A. Vaidya, A. Gouldstone, S. Sampath, Non-linear elastic properties of plasma-sprayed zirconia coatings and associated relationships with processing conditions, Acta Mater. 55 (14) (2007) 4667–4678, http://dx.doi.org/10.1016/j.actamat.2007.04.037.

[15] D. Lal, P. Kumar, R. Bathe, S. Sampath, V. Jayaram, Effect of microstructure on fracture behavior of freestanding plasma sprayed 7 wt.% Y2O3 stabilized ZrO2, J. Eur. Ceram. Soc. 41 (7) (2021) 4294–4301, http://dx.doi.org/10.1016/j.jeurceramsoc.2021.02.038.

[16] R. Musalek, J. Matejicek, M. Vilemova, O. Kovarik, Non-linear mechanical behavior of plasma sprayed alumina under mechanical and thermal loading, J. Therm. Spray Tech. 19 (1–2) (2010) 422–428, http://dx.doi.org/10.1007/s11666-009-9362-x.

[17] S. Patibanda, V. Nagda, J. Kalra, G. Sivakumar, R. Abrahams, K. Jonnalagadda, Mechanical behavior of freestanding 8YSZ thin films under tensile and bending loads, Surf. Coat. Technol. 393 (2020) 125771, http://dx.doi.org/10.1016/j.surfcoat.2020.125771.

[18] I. Sevostianov, M. Kachanov, Modeling of the anisotropic elastic properties of plasma-sprayed coatings in relation to their microstructure, Acta Mater. 48 (6) (2000) 1361–1370, http://dx.doi.org/10.1016/S1359-6454(99)00384-5.

[19] F. Kroupa, J. Plesek, Nonlinear elastic behavior in compression of thermally sprayed materials, Mater. Sci. Eng. A 328 (1–2) (2002) 1–7, http://dx.doi.org/10.1016/S0921-5093(01)01653-7.

[20] R. Zhao, C. Li, Porosity-dependent velocities of longitudinal and transverse waves in dry porous materials, Appl. Acoust. 176 (2021) 107757, http://dx.doi.org/10.1016/j.apacoust.2020.107757.

[21] G. Bruno, M. Kachanov, Microstructure-property connections for porous ceramics: The possibilities offered by micromechanics, J. Am. Ceram. Soc. 99 (12) (2016) 3829–3852, http://dx.doi.org/10.1111/jace.14624.

[22] T. Nakamura, G. Qian, C.C. Berndt, Effects of pores on mechanical properties of plasma-sprayed ceramic coatings, J. Am. Ceram. Soc. 83 (3) (2004) 578–584, http://dx.doi.org/10.1111/j.1151-2916.2000.tb01236.x.

[23] R. Bolot, D. Aussavy, G. Montavon, Application of FEM to estimate thermo-mechanical properties of plasma sprayed composite coatings, Coatings 7 (7) (2017) 91, http://dx.doi.org/10.3390/coatings7070091.

[24] J.-H. Qiao, R. Bolot, H. Liao, Finite element modeling of the elastic modulus of thermal barrier coatings, Surf. Coat. Technol. 220 (2013) 170–173, http://dx.doi.org/10.1016/j.surfcoat.2012.05.031.

[25] O. Amsellem, K. Madi, F. Borit, D. Jeulin, V. Guipont, M. Jeandin, E. Boller, F. Pauchet, Two-dimensional (2D) and three-dimensional (3D) analyses of plasma-sprayed alumina microstructures for finite-element simulation of Young's modulus, J. Mater. Sci. 43 (12) (2008) 4091–4098, http://dx.doi.org/10.1007/s10853-007-2239-9.

[26] W. Zeng, Y.-F. Ye, Z.-M. Kuang, W.-L. Tian, Three-dimensional model reconstruction and numerical simulation of the jointed rock specimen under conventional triaxial compression, Num. Anal. Meth. Geomechan. 46 (10) (2022) 1851–1873, http://dx.doi.org/10.1002/nag.3371.

[27] J.A. Taillon, C. Pellegrinelli, Y.-L. Huang, E.D. Wachsman, L.G. Salamanca-Riba, Improving microstructural quantification in FIB/SEM nanotomography, Ultramicroscopy 184 (2018) 24–38, http://dx.doi.org/10.1016/j.ultramic.2017.07.017.

[28] A. Abaza, J. Laurencin, A. Nakajo, M. Hubert, T. David, F. Monaco, C. Lenser, S. Meille, Fracture properties of porous yttria-stabilized zirconia under micro-compression testing, J. Am. Ceram. Soc. 42 (4) (2022) 1656–1669, http://dx.doi.org/10.1016/j.jeurceramsoc.2021.11.051.

[29] M. Sharafisafa, M. Nazem, Application of the distinct element method and the extended finite element method in modelling cracks and coalescence in brittle materials, Comput. Mater. Sci. 91 (2014) 102–121, http://dx.doi.org/10.1016/j.commatsci.2014.04.006.

[30] P.A. Cundall, O.D.L. Strack, A discrete numerical model for granular assemblies, Géotechnique 29 (1) (1979) 47–65, http://dx.doi.org/10.1680/geot.1979.29.1.47.

[31] K. Marchais, J. Girardot, C. Metton, I. Iordanoff, A 3D DEM simulation to study the influence of material and process parameters on spreading of metallic powder in additive manufacturing, Comp. Part. Mech. 8 (4) (2021) 943–953, http://dx.doi.org/10.1007/s40571-020-00380-z.

[32] D.O. Potyondy, P.A. Cundall, A bonded-particle model for rock, Int. J. Rock Mech. Min. Sci. 41 (2004) 1329–1364, http://dx.doi.org/10.1016/j.ijrmms.2004.09.011.

[33] W. Leclerc, H. Haddad, M. Guessasma, On the suitability of a discrete element method to simulate cracks initiation and propagation in heterogeneous media, Int. J. Solids Struct. 108 (2017) 98–114, http://dx.doi.org/10.1016/j.ijsolstr.2016.11.015.

[34] K. Radi, D. Jauffrès, S. Deville, C.L. Martin, Elasticity and fracture of brick and mortar materials using discrete element simulations, J. Mech. Phys. Solids 126 (2019) 101–116, http://dx.doi.org/10.1016/j.jmps.2019.02.009.

[35] F. Asadi, D. André, S. Emam, P. Doumalin, M. Huger, Numerical modelling of the quasi-brittle behaviour of refractory ceramics by considering microcracks effect, J. Am. Ceram. Soc. 42 (3) (2022) 1149–1161, http://dx.doi.org/10.1016/j.jeurceramsoc.2021.11.016.

[36] N. Ferguen, Y. Mebdoua-Lahmar, H. Lahmar, W. Leclerc, M. Guessasma, DEM model for simulation of crack propagation in plasma-sprayed alumina coatings, Surf. Coat. Technol. 371 (2019) 287–297, http://dx.doi.org/10.1016/j.surfcoat.2018.07.065.

[37] K. Radi, H. Saad, D. Jauffres, S. Meille, T. Douillard, S. Deville, C.L. Martin, Effect of microstructure heterogeneity on the damage resistance of nacre-like alumina: Insights from image-based discrete simulations, Scr. Mater. 191 (2021) 210–214, http://dx.doi.org/10.1016/j.scriptamat.2020.09.034.

[38] D. Roussel, A. Lichtner, D. Jauffrès, J. Villanova, R.K. Bordia, C.L. Martin, Strength of hierarchically porous ceramics: Discrete simulations on X-ray nanotomography images, Scr. Mater. 113 (2016) 250–253, http://dx.doi.org/10.1016/j.scriptamat.2015.11.015.

[39] Y. Wang, P. Mora, Modeling wing crack extension: Implications for the ingredients of discrete element model, Pure appl. geophys. 165 (3–4) (2008) 609–620, http://dx.doi.org/10.1007/s00024-008-0315-y.

[40] J. Duriez, L. Scholtès, F.-V. Donzé, Micromechanics of wing crack propagation for different flaw properties, Eng. Fract. Mech. 153 (2016) 378–398, http://dx.doi.org/10.1016/j.engfracmech.2015.12.034.

[41] X. Chen, C. Shi, H.-N. Ruan, W.-K. Yang, Numerical simulation for compressive and tensile behaviors of rock with virtual microcracks, Arab. J. Geosci. 14 (10) (2021) 870, http://dx.doi.org/10.1007/s12517-021-07163-7.

[42] P.-Q. Ji, X.-P. Zhang, Q. Zhang, A new method to model the non-linear crack closure behavior of rocks under uniaxial compression, Int. J. Rock Mech. Min. Sci. 112 (2018) 171–183, http://dx.doi.org/10.1016/j.ijrmms.2018.10.015.

[43] X. Zhang, B. Fatahi, H. Khabbaz, Investigating effects of fracture aperture and orientation on the behaviour of weak rock using discrete element method, in: L. Zhang, B. Goncalves Da Silva, C. Zhao (Eds.), Proceedings of GeoShanghai 2018 International Conference: Rock Mechanics and Rock Engineering, Springer Singapore, Singapore, 2018, pp. 74–81, http://dx.doi.org/10.1007/978-981-13-0113-1_9.

[44] Y. Ye, Y. Zeng, S. Cheng, X. Chen, H. Sun, Three-dimensional DEM simulation of the nonlinear crack closure behaviour of rocks, Num. Anal. Meth. Geomechan. 46 (10) (2022) 1956–1971, http://dx.doi.org/10.1002/nag.3376.

[45] M. Fu, G.-F. Zhao, A micro-macro constitutive model for compressive failure of rock by using 4D lattice spring model, Int. J. Rock Mech. Min. Sci. 160 (2022) 105261, http://dx.doi.org/10.1016/j.ijrmms.2022.105261.

[46] A. Selçuk, A. Atkinson, Elastic properties of ceramic oxides used in solid oxide fuel cells (SOFC), J. Eur. Ceram. 17 (12) (1997) 1523–1532, http://dx.doi.org/10.1016/S0955-2219(96)00247-6.

[47] A. Buades, B. Coll, J.-M. Morel, A non-local algorithm for image denoising, in: 2005 IEEE Computer Society Conference on Computer Vision and Pattern Recognition. Vol. 2, CVPR'05, IEEE, San Diego, CA, USA, 2005, pp. 60–65, http://dx.doi.org/10.1109/CVPR.2005.38.

[48] N. Otsu, A threshold selection method from gray-level histograms, IEEE Trans. Syst. Man Cybern. 9 (1) (1979) 62–66, http://dx.doi.org/10.1109/TSMC.1979.4310076.

[49] P. Sahoo, S. Soltani, A. Wong, A survey of thresholding techniques, Comput. Vis. Graph. Image Process. 41 (2) (1988) 233–260, http://dx.doi.org/10.1016/0734-189X(88)90022-9.

[50] W.-H. Tsai, Moment-preserving thresolding: A new approach, Comput. Vis. Graph. Image Process. 29 (3) (1985) 377–393, http://dx.doi.org/10.1016/0734-189X(85)90133-1.

[51] G. Antou, G. Montavon, F. Hlawka, A. Cornet, C. Coddet, Characterizations of the pore-crack network architecture of thermal-sprayed coatings, Mater. Charact. 53 (5) (2004) 361–372, http://dx.doi.org/10.1016/j.matchar.2004.08.015.

[52] H. Edelsbrunner, E.P. Mücke, Three-dimensional alpha shapes, in: Proceedings of the 1992 Workshop on Volume Visualization, VVS '92, ACM Press, Boston, Massachusetts, United States, 1992, pp. 75–82, http://dx.doi.org/10.1145/147130.147153.

[53] P. Cignoni, M. Callieri, M. Corsini, M. Dellepiane, F. Ganovelli, G. Ranzuglia, MeshLab: An open-source mesh processing tool, in: Eurographics Italian Chapter Conference, The Eurographics Association, 2008, pp. 129–136, http://dx.doi.org/10.2312/LocalChapterEvents/ItalChap/ItalianChapConf2008/129-136.

[54] D. André, I. Iordanoff, J.-l. Charles, J. Néauport, Discrete element method to simulate continuous material by using the cohesive beam model, Comput. Methods Appl. Mech. Engrg. 213–216 (2012) 113–125, http://dx.doi.org/10.1016/j.cma.2011.12.002.

[55] M. Sage, J. Girardot, J.-B. Kopp, S. Morel, A damaging beam-lattice model for quasi-brittle fracture, Int. J. Solids Struct. 239–240 (2022) 111404, http://dx.doi.org/10.1016/j.ijsolstr.2021.111404.

[56] T. Pazmiño, I. Pombo, J. Girardot, L. Godino, J. Sánchez, Multiscale simulation of volumetric wear of vitrified alumina grinding wheels, Wear 530–531 (2023) 205020, http://dx.doi.org/10.1016/j.wear.2023.205020.

[57] U. Welling, G. Germano, Efficiency of linked cell algorithms, Comput. Phys. Comm. 182 (3) (2011) 611–615, http://dx.doi.org/10.1016/j.cpc.2010.11.002.

[58] R. Danzer, P. Supancic, J. Pascual, T. Lube, Fracture statistics of ceramics – Weibull statistics and deviations from Weibull statistics, Eng. Fract. Mech. 74 (18) (2007) 2919–2932, http://dx.doi.org/10.1016/j.engfracmech.2006.05.028.

[59] S. Parthasarathi, B.R. Tittmann, K. Sampath, E.J. Onesto, Ultrasonic characterization of elastic anisotropy in plasma-sprayed alumina coatings, J. Therm. Spray Technol. 4 (4) (1995) 367–373, http://dx.doi.org/10.1007/BF02648637.

[60] Y. Tan, A. Shyam, W. Choi, E. Lara-Curzio, S. Sampath, Anisotropic elastic properties of thermal spray coatings determined via resonant ultrasound spectroscopy, Acta Mater. 58 (16) (2010) 5305–5315, http://dx.doi.org/10.1016/j.actamat.2010.06.003.

[61] H. Echsler, D. Renusch, M. Schütze, Mechanical behaviour of as sprayed and sintered air plasma sprayed partially stabilised zirconia, J. Mater. Sci. Technol. 20 (7) (2004) 869–876, http://dx.doi.org/10.1179/026708304225017346.

[62] A.V. Manoylov, F.M. Borodich, H.P. Evans, Modelling of elastic properties of sintered porous materials, Proc. R. Soc. A. 469 (2154) (2013) 20120689, http://dx.doi.org/10.1098/rspa.2012.0689.

[63] D. André, M. Jebahi, I. Iordanoff, J.-l. Charles, J. Néauport, Using the discrete element method to simulate brittle fracture in the indentation of a silica glass with a blunt indenter, Comput. Methods Appl. Mech. Engrg. 265 (2013) 136–147, http://dx.doi.org/10.1016/j.cma.2013.06.008.